

Article

The Influence of Platen Stiffness on a Specimen's Failure Initiation Point and the Failure Pattern of Brittle Materials in the Standardized Uniaxial Compression Test

Diego-José Guerrero-Miguel ^{1,*}, Martina-Inmaculada Álvarez-Fernández ¹, Ramón Gutiérrez-Moizant ²,
María-Belén Prendes-Gero ¹ and Celestino González-Nicieza ¹

¹ DinRock Group, Universidad de Oviedo, 33004 Oviedo, Asturias, Spain;
inma@dinrock-uniovi.com (M.-I.Á.-F.); belen@dinrock-uniovi.com (M.-B.P.-G.);
celestino@dinrock-uniovi.com (C.G.-N.)

² Mechanical Engineering Department, Universidad Carlos III de Madrid, 28911 Leganés, Madrid, Spain;
ragutier@ing.uc3m.es

* Correspondence: diego@dinrock-uniovi.com

Abstract: Uniaxial compressive strength is a variable necessary for adequately characterizing a material's mechanical properties. However, a specimen's geometric deviations and elastic properties may lead to undesirable stress states, which cause strong discrepancies between the results of the uniaxial compression test and its theoretical foundations. While geometric deviations may cause non-uniform contact between the platen and the specimen, elastic properties can provoke severe end effects that disturb the local stress field near the points of contact. To address how the relative stiffness between the platen and the specimen influences the induced stress field, numerical simulations considering the stiffness ratios $E_p/E_s = 3$, $E_p/E_s = 1$ and $E_p/E_s = 0.05$ were performed. Subsequently, these results were employed to establish the relation between relative stiffness and specimen failure patterns in brittle materials, particularly in three different rocks. The results prove that the platen stiffness must be accurately selected to match that of the tested material, in order to avoid undesirable local stress fields near the point of contact and to induce homogeneous uniaxial compression that guarantees reliable uniaxial compressive strength characterization. Furthermore, the brittle failure patterns reported in previous studies were correlated with the induced stress fields inside the specimen depending on its platen stiffness, allowing the validity of the test results to be verified based on a simple visual inspection.

Keywords: relative stiffness; length-to-diameter ratio; uniaxial compressive strength; elastic behavior; brittle failure

MSC: 65Z05



Citation: Guerrero-Miguel, D.-J.; Álvarez-Fernández, M.-I.; Gutiérrez-Moizant, R.; Prendes-Gero, M.-B.; González-Nicieza, C. The Influence of Platen Stiffness on a Specimen's Failure Initiation Point and the Failure Pattern of Brittle Materials in the Standardized Uniaxial Compression Test. *Mathematics* **2024**, *12*, 907. <https://doi.org/10.3390/math12060907>

Academic Editor: Lihua Wang

Received: 27 January 2024

Revised: 19 February 2024

Accepted: 26 February 2024

Published: 20 March 2024



Copyright: © 2024 by the authors. Licensee MDPI, Basel, Switzerland. This article is an open access article distributed under the terms and conditions of the Creative Commons Attribution (CC BY) license (<https://creativecommons.org/licenses/by/4.0/>).

1. Introduction

The accurate characterization of a material's mechanical properties is mandatory to successfully determine its strength and, consequently, its suitability for specific engineering projects and applications. This requirement not only applies to manufactured materials employed in industrial products, but also to naturally generated ones such as rock materials, which are involved in engineering projects related to underground work, mining or civil topics. Consequently, a precise characterization is usually required to determine the capabilities of a given material subjected to various stress conditions. To achieve this, its tensile, compressive and triaxial strengths at different stress ratios must be obtained.

In the case of ductile materials, it is common to subject a specimen to direct tensile tests. However, for brittle materials, any limitations to achieving the desired dog-bone shape during the specimen preparation process or the possibility of inducing cracks when

fixing the specimen to the testing device mean that an indirect tensile test [1–8], also known as the Brazilian test [9], is still preferred. Nevertheless, new procedures to determine the uniaxial tensile strength (UTS) are increasing in popularity [10,11], as they provide a true uniaxial stress state (UTS) rather than a combined biaxial one [12,13].

The determination of the uniaxial compressive strength (UCS) is typically performed using the standardized uniaxial compression test (UCT), employing prismatic or cylindrical geometries for most materials [14–20]. Nevertheless, indirect methods, such as the point load test [21–24] or the Schmidt–Hammer test [25,26], are becoming increasingly popular, as no particular standardized geometry shape must be reproduced; this is extremely useful in those cases where the available samples can be limited or difficult to obtain due to location.

Although the UCT has been meticulously standardized by several societies and institutions to ensure its trustworthiness and reliability, discrepancies between its theoretical foundations and the expected experimental results have been documented. From an elastic perspective, the material considered is subject to a uniform compression stress along the contact between the specimen and the platens, which induces a homogeneous compressive stress field inside the specimen. However, it is widely accepted that in the vicinity of the contact, a non-homogeneous triaxial stress field is generated due to shear stresses caused by the different stiffness values between the materials of the platen and specimen. Notably, these shear stresses may evolve into friction when the applied load allows slippery contact conditions to be induced. Several theoretical formulations seek to capture this end-effect phenomenon [27–29]; however, the influence of constrained displacement at end points is still under discussion among the scientific community. In this sense, different slenderness ratios have been proposed to limit its influence [30–32]. Nevertheless, consensus on the relative stiffness of post-peak behavior exists, which is considered to be dependent on the friction between the platen and the specimen, instead of being an intrinsic property of the tested material [31,33].

All of these discrepancies may explain the variability in the accepted failure patterns related to the UCT [34,35], although the specific testing conditions responsible for them remain uncertain. It is worth highlighting here that some discrepancies may also exist in the characterization of elastic constants depending on the measuring technique employed, although novel research directions currently allow the results between procedures to be corrected [36–38].

The material strength for confined stress states is addressed by the triaxial compression test. It is conducted using a Hoek cell; not only are stresses on the ends of a cylindrical specimen applied, but a uniform fluid pressure is also applied to its lateral surface [39,40]. Thus, by selecting adequate ratios between the axial and confining stresses, the material's behavior can be predicted. Nevertheless, this test implies that the minor (σ_3) and intermediate (σ_2) principal stresses are equal; thus, deviations from the triaxial test results must be expected when this requirement is not fulfilled [41,42].

To determine a material's strength under real-world conditions, failure envelopes must be obtained by combining the results from a Brazilian test, a uniaxial compression test and a triaxial compression test. The failure envelopes of brittle materials are usually established by means of the Mohr–Coulomb or Hoek–Brown criterion [39,43]. The former considers a linear relationship between the major (σ_1) and minimum (σ_3) principal stresses, whereas the second establishes a non-linear envelope, as shown in Equations (1) and (2), where ϕ is the friction coefficient and m and s are material constants, setting $s = 1$ for the case of an intact rock.

$$\sigma_1 = \frac{1 + \sin \phi}{1 - \sin \phi} \sigma_3 + UCS \quad (1)$$

$$\sigma_1 = \sigma_3 + UCS \left(m \frac{\sigma_3}{UCS} + s \right)^{0.5} \quad (2)$$

It is worth highlighting that the sign criterion used relates to compressive and tensile stresses as positive and negative stress values, respectively, as is commonly used in the field of rock mechanics. Nevertheless, it is pertinent to emphasize that the Mohr–Coulomb

criterion is mainly formulated to address the compressive area ($\sigma_3 > 0$) of the $\sigma_1 - \sigma_3$ chart (Figure 1). Hence, its straightforward lengthening into the tensile area ($\sigma_3 < 0$) would lead to excessively imprecise results. To soften this limitation, a truncated Mohr–Coulomb (TMC) criterion is used instead (Figure 1), which restricts the allowable tensile states ($\sigma_3 < 0$) to those under the maximum threshold value set by the indirect tensile strength obtained in the Brazilian test (σ_{BD}). Therefore, the compressive and tensile values are encompassed in a more consistent failure envelope.

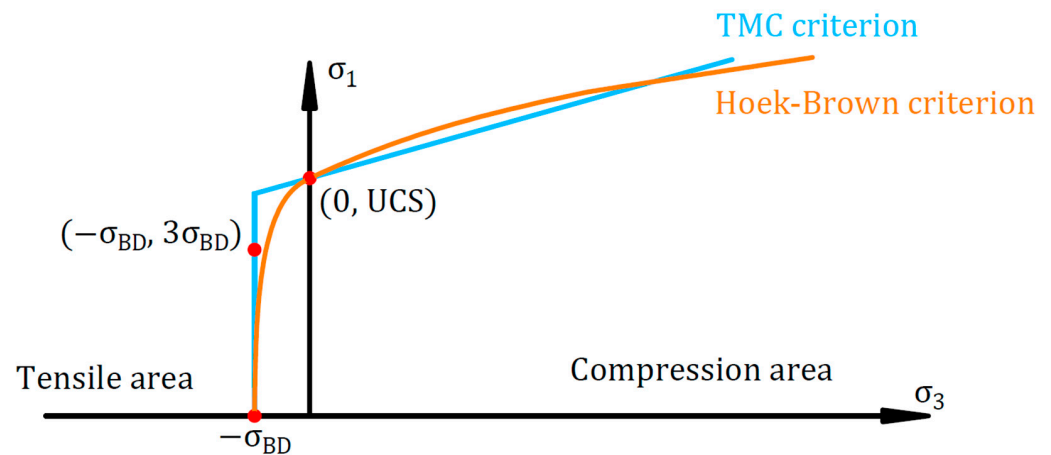


Figure 1. Truncated Mohr–Coulomb and Hoek–Brown criteria.

This approach is conservative for bearing purposes, as elastic theory guarantees higher tensile σ_3 values before reaching failure. In this sense, the Hoek–Brown criterion is even more conservative, as it equates the indirect tensile strength with the uniaxial one, thereby transforming the point $(\sigma_3, \sigma_1 = -\sigma_{BD}, 3\sigma_{BD})$ into $(\sigma_3, \sigma_1 = -\sigma_{BD}, 0)$.

Due to the relevance of accurately determining UCS for engineering purposes, the influence of relative stiffness in the induced stress field inside the specimen is investigated to ascertain UCT suitability to generate homogeneous compression fields. For this purpose, numerical UCT simulations considering ratios between the platen (E_p) and specimen (E_s) stiffnesses of 3, 1 and 0.05 were performed. Subsequently, and based on the induced stress fields obtained, the location of the failure initiation point for brittle materials and its correlation with main failure patterns registered in the current literature are discussed. The results highlight that uniaxial compression stress states at the failure initiation point are only guaranteed for platens with similar stiffness to the tested specimen, and that brittle failure patterns depend on relative stiffness.

2. Numerical Model

To address the influence of relative stiffness between the platen and the specimen in the output results obtained from the standardized UCT, numerical simulations were performed using the commercial software FLAC 7 3D version 7.00, which is widely used in the field of rock mechanics modeling [44]. Therefore, the elastic behavior was predicted using a finite difference method (FDM) [45,46]. The latter is based on substituting the partial derivatives of a desired function by finite differences on a given domain [44]. Hence, the continuity of this method's results is one of its essential characteristics, but it also reveals one of its major drawbacks, which is that it does not adequately address fractures in the material. The materials in our proposed analysis were limited to the elastic range, with no damage evolution, as only the failure initiation point was determined; FDM therefore remains a suitable choice to model the UCT for our stated purposes.

Standards suggest different acceptable length (L)-to-diameter (D) ratios for the tested specimens. Nevertheless, the obtained results can be considered acceptable if the aspect ratio (L/D) is between 2 and 3. Indeed, a value of $L/D = 2.5$ is simultaneously proposed by main rock mechanics standards. For this reason, the specimen used in the numerical model

is 50 mm in diameter and 125 mm in length. It can be argued that such dimensions do not strictly fulfill the minimum 54 mm diameter standard. Nevertheless, this recommendation is due to the intrinsic heterogeneity of most rock materials, in which grain sizes of several millimeters may behave as large inclusions, and thus cause the test results to deviate.

Regarding the platen dimensions, they were all 50 mm in diameter and 40 mm in thickness to ensure that most standards were simultaneously satisfied.

As the geometries used in the numerical model are theoretically perfect—their shape exactly matches that of ideal cylinders—no further considerations regarding geometric deviations were made. However, this limits the results to the case in which specimen ends can be considered perfectly flat for practical purposes.

All the specimens and platens were considered to be homogeneous and isotropic materials. Furthermore, as the current research addresses the failure of brittle materials, their plastic behavior was considered neglectable; therefore, the specimens had perfectly elastic behavior up to the initiation of failure.

On each mesh element, the stress state can be defined by their maximum (σ_1), intermediate (σ_2) and minimum (σ_3) principal stresses and their directions. However, as only σ_1 and σ_3 are considered in most applied failure criteria for brittle materials, the σ_2 values will be neglected in subsequent sections of this article.

To accurately reproduce the contact phenomenon reported during test execution, we only imposed displacements as boundary conditions. Hence, instead of distributing stresses along the contact surfaces in an arbitrary manner, the top of the upper plate ($y = 102.5$ mm) was displaced towards the specimen with a velocity of 10^{-10} m/s, in order for equilibrium conditions to be fulfilled between each calculation step. No other restrictions or assumptions were made on the shear stresses or horizontal displacements at the surface of the top platen. Under this approach, stresses are induced inside the specimen due to the compression caused by the platen during its displacement. Although the use of an interphase is widely accepted as the means to solve the problem under certain contact restrictions, the authors consider that it may cause biased results, as many assumptions may not necessarily hold true during real test executions. For this reason, the simulation was performed without the use of interphase between the elastic bodies. Contrarily, the model was meshed, assigning a common node for the specimen and the platen points in contact. Consequently, the results are limited to those cases where neither slippery nor relative horizontal displacement between contact surfaces is allowed. Hence, this analysis cannot be extended to the case of friction or the use of effective lubricants.

The addressed problem is elastically three-dimensional; however, considering that platens and the specimen are perfect solids of revolution and that contact conditions have radial symmetry, the problem can be treated as an axisymmetric one. Therefore, the stress state on each element is independent of its angular position; thus, only 45° of the cylinders were used as geometric input to the model (Figure 2).

The mechanical properties of the assigned materials, as well as the ratio that relates the platen (E_p) and specimen (E_s) Young's modulus and Poisson's ratio (ν), are shown in Table 1. The M2 material properties were elected to match representative values of rock materials [40], whereas M1 and M3 were aimed at representing a much stiffer material and an extensively softer one, respectively. For this purpose, mechanical properties similar to those of steel and polymethyl methacrylate were selected [47].

Table 1. Mechanical properties of the material assigned to the model.

	Stiffer Platen M1	Equal Stiffness Platen M2	Less Stiff Platen M3
Young's Modulus E (GPa)	210	70	3.20
Poisson's ratio	0.30	0.33	0.40
E_p/E_s	3	1	0.05

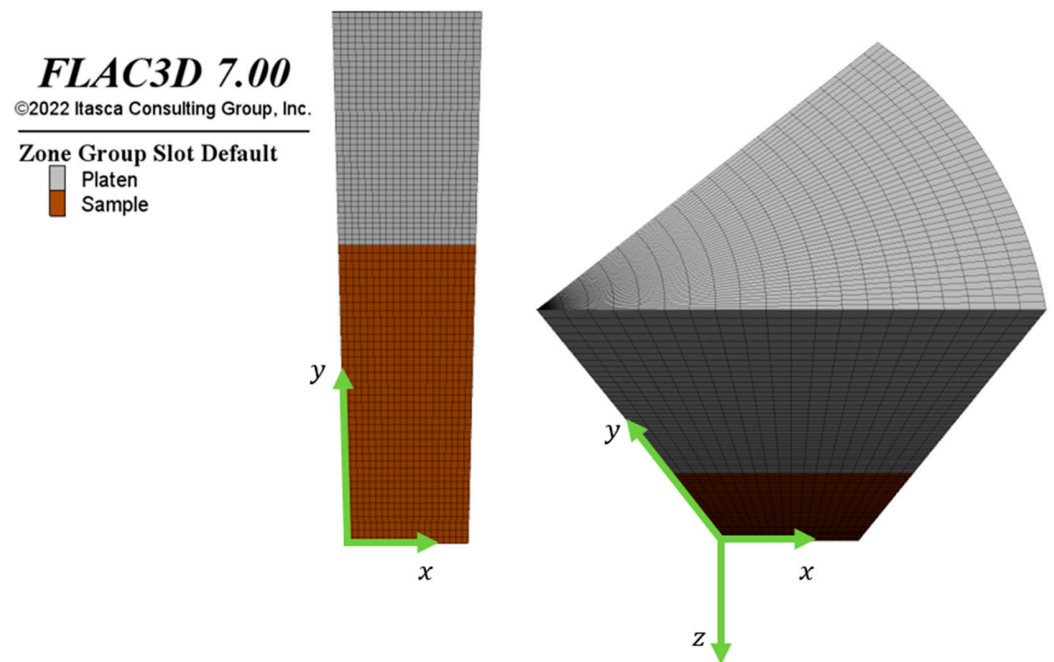


Figure 2. Model used for the numerical simulations.

Additionally, to address the influence of platen stiffness on the failure initiation point, as well as in the associated failure pattern, three different limestone lithotypes were used [48]. These limestones were selected to cover a wide spectrum of different UCS, σ_{BD} and ϕ values, as shown in Table 2.

Table 2. Mechanical properties of the rocks employed to determine the failure initiation point. Data are extracted from reference [48].

	Limestone Lithotype L1	Limestone Lithotype L2	Limestone Lithotype L3
Uniaxial compressive strength UCS (MPa)	83.0	42.7	52.4
Internal friction angle ϕ ($^{\circ}$)	37.4	35.3	27.3
Indirect tensile strength σ_{BD}	5.5	2.8	3.2

A new stress defined as σ_0 , equal to 70% of the limestone lithotype 2 UCS value, was selected to normalize all of the stress states and simultaneously ensure that the results were limited to the elastic range. Once the σ_0 value was reached in the points of the outer circumference, the platen stopped its movement.

3. Platen Stiffness Influence on Stress Field inside the Specimen

Due to the strain mismatch for a given load between platen and specimen materials, shearing stresses appeared in their contact surfaces. Therefore, different platens will inevitably lead to different contact stress distributions and, consequently, to different induced stress fields inside the specimen. In this section, a detailed analysis was performed to highlight the main differences when significantly higher, almost equal, and significantly lower platen stiffnesses are used. For this purpose, platens with stiffness ratios of $E_p/E_s = 3$, $E_p/E_s = 1$ and $E_p/E_s = 0.05$ were simulated. It is worth remembering here that aluminum was assigned as a specimen material in the numerical model for its well-known and representative elastic properties. Special attention was paid to points where pure compression

($\sigma_3 = 0$ and $\sigma_1 > 0$) or pure tensile stress states ($\sigma_3 < 0$ and $\sigma_1 = 0$) were induced. In addition, the evolution of the maximum shearing stresses (τ_{max}) for each case is discussed.

3.1. Stress Field Comparison

In light of the previous discussion, it follows that relative stiffness significantly influences the stress field generated inside the specimen, especially in the vicinity of contact. The stress states for all of the mesh elements and for all considered platens are depicted in Figure 3. The distribution of stress states plotted in the $\sigma_1 - \sigma_3$ charts substantially varies for each stiffness ratio; this allows for straightforward identification of the platen used from its particular $\sigma_1 - \sigma_3$ chart shape (Figure 3). In those cases where a significant difference in relative stiffness exists, the stress field is strongly influenced by the appearance of σ_3 stresses that cause a deviation from the desired homogeneous uniaxial compression field inside the specimen. Regarding this phenomenon, the ratio $E_p/E_s = 3$ principally induces σ_3 compression stresses, whereas the latter are principally tensile for $E_p/E_s = 0.05$. In this sense, as brittle materials tend to show lower tensile than compressive strength values, stiffer platens may be preferable to use for test execution, thus avoiding local tensile failures near the contact.

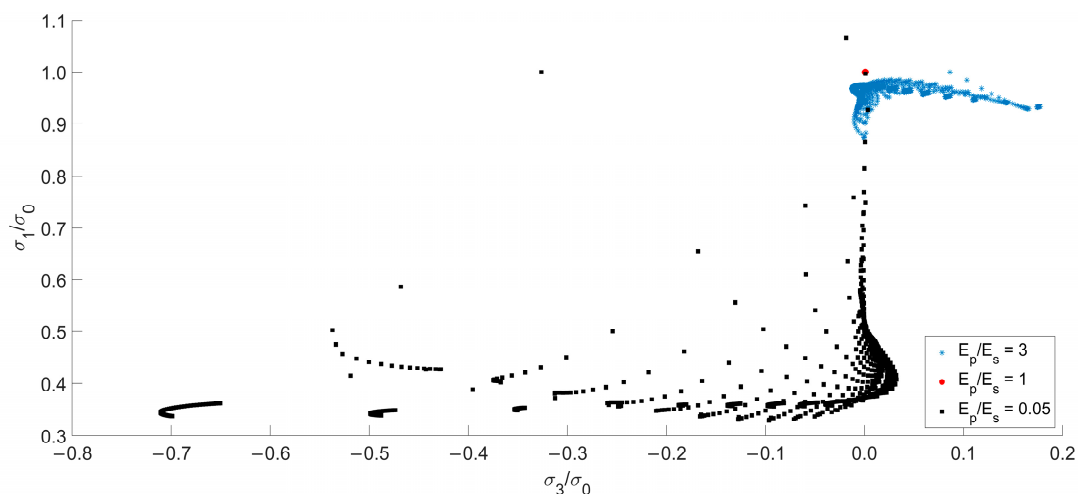


Figure 3. Stress field inside the specimen for the case of stiffer $E_p/E_s = 3$, equal ($E_p/E_s = 1$) and softer ($E_p/E_s = 0.05$) platens.

However, the dispersion of stress states among the $\sigma_1 - \sigma_3$ chart almost vanished for platens with similar stiffnesses to the tested specimen ($E_p/E_s = 1$), as shown in Figure 3. Indeed, for practical applications, the dispersion can be considered reduced to just one point located along the σ_1 axis. In other words, no tensile stress is involved in the induced stress field, and a unique compression stress value is induced to the whole specimen. Given that the main purpose of the UCT is to accurately determine the UCS, it is imperative to minimize the influence of σ_3 values, either tensile or compressive, as they cause the induced stress field to deviate from the desired uniaxial compression field. Consequently, more coherent results are obtained regarding the theoretical assumptions from the test using the $E_p/E_s = 1$ ratio for the platens.

As in any numerical model, minor rounding discrepancies with respect to the analytic solutions may arise. Consequently, and aiming at a practical application of the obtained data, values of $\sigma_3 < 0.001\sigma_{1max}$ were considered as pure compression ($\sigma_3 = 0$ and $\sigma_1 > 0$) in the subsequent analysis.

Figure 4 illustrates all of the different stress states generated across the spectrum of platen stiffnesses under consideration: pure compression ($\sigma_1 > 0$ and $\sigma_3 = 0$) is represented by red points, the σ_3 tensile component with green ones, and cases with both maximum (σ_1) and minimum (σ_3) stress components of compression are depicted with blue dots. Regarding softer platens ($E_p/E_s = 0.05$), all points in the medium transversal plane

develop a tensile stress lower than $0.002\sigma_{1_{max}}$; therefore, they do not satisfy the imposed requirement for pure compression. Nevertheless, they prove that stiffness conditions have no influence on the induced stress state at points located far from the contact (Figure 4). Thus, pure compression is distributed along the mid height of the specimen for all cases, making it reasonable to accept that a local uniaxial compression stress field exists in this area independently from the platen stiffness. However, this last statement must be considered cautiously, as only one length-to-diameter ratio of $L/D = 2.5$ was considered.

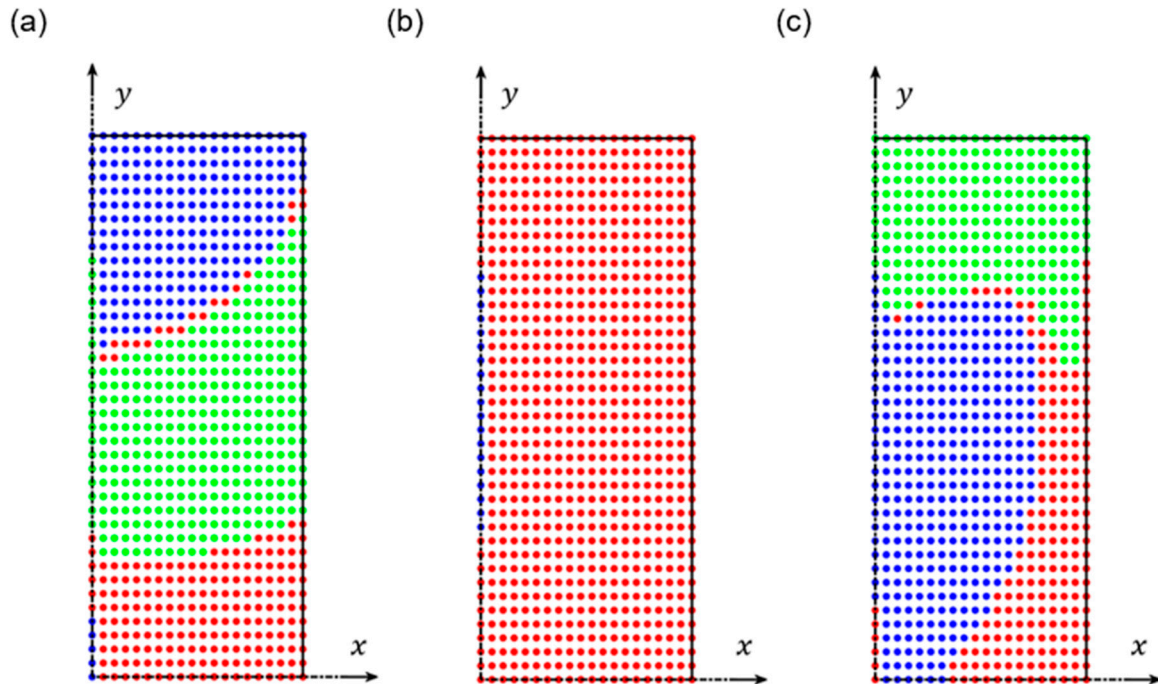


Figure 4. Areas with pure compression (red), tensile σ_3 (green) and double compression (blue) for the cases of (a) $E_p/E_s = 3$, (b) $E_p/E_s = 1$ and (c) $E_p/E_s = 0.05$.

Furthermore, equal stiff platens ($E_p/E_s = 1$) induce a stress field with a ratio between maximum and minimum compressive stresses ($\sigma_{1_{max}}$ and $\sigma_{1_{min}}$, respectively) of $\sigma_{1_{min}}/\sigma_{1_{max}} = 0.99$ and neglectable σ_3 . Therefore, it was found that a uniaxial compression stress field inside the specimen is guaranteed for stiffness ratios close to $E_p/E_s = 1$. Hence, no further considerations were made on tensile stresses for this case, as they could be neglected for practical purposes.

Special attention must be paid to the tensile σ_3 areas depicted in Figure 4. They appeared for both stiffer ($E_p/E_s = 3$) and softer ($E_p/E_s = 0.05$) platens; however, the induced stress states strongly differed in each case. Whereas the former generate tensile stresses in points located far from the contact, they are placed in its immediate vicinity for the latter. Both cases can be considered almost complementary to each other, for which the distribution of tensile stress points refers to inside the specimen.

Despite similarities shown in the specimen's mid height (Figure 4), the $E_p/E_s = 3$ and $E_p/E_s = 0.05$ ratios strongly differ on the stress state induced in the points located at the vicinity of the contact. Whereas the former generate a compressive bulb in which both stress components (σ_1 and σ_3) are compressive (blue dots in Figure 4), the latter generates tensile stresses (green dots in Figure 4) due to the higher deformation of the platen, which is a softer material than the tested specimen (Figure 4). Nevertheless, it must be noted that these discrepancies regarding the comparison of the $E_p/E_s = 3$ and $E_p/E_s = 0.05$ ratios should only be applied for specimens with an aspect ratio of $L/D = 2.5$. For lower L/D values, the aforementioned bulbs may be close enough to meet each other and, therefore, the existence of points with a uniaxial compressive state would be reduced. Determining the exact highest aspect ratio where this phenomenon is first produced is beyond the scope

of the present study, as only the influence of relative stiffness and not of the slenderness ratio was considered. However, its dependence on the relative stiffness is undoubtedly based on the exposed results.

3.2. Identification of Relevant Points on the $\sigma_1 - \sigma_3$

Figure 5 shows the stress field induced by stiffer platens ($E_p/E_s = 3$) across the whole specimen. It is worth noting that there are two sets of points of special interest—those related to elevated σ_1 values that form a straight line with a negative slope in the $\sigma_1 - \sigma_3$ chart (highlighted in purple in Figure 5), and those with σ_3 tensile values located on the tensile bulb highlighted in green in Figure 5. The former belong to the top and bottom ends of the specimen, where the maximum σ_1 value (highlighted in red) is simultaneously located on their outer circumference. This decreasing slope is of special interest, as it proves that compressive stresses along the contact may not be uniformly distributed along it, being maximum at the vicinity of the lateral surface and decreasing towards the centre of both ends. Furthermore, points belonging to the tensile bulb (highlighted in green on Figure 5) are all located along the longitudinal axis of the specimen, which suggests that its failure may be initiated along it.

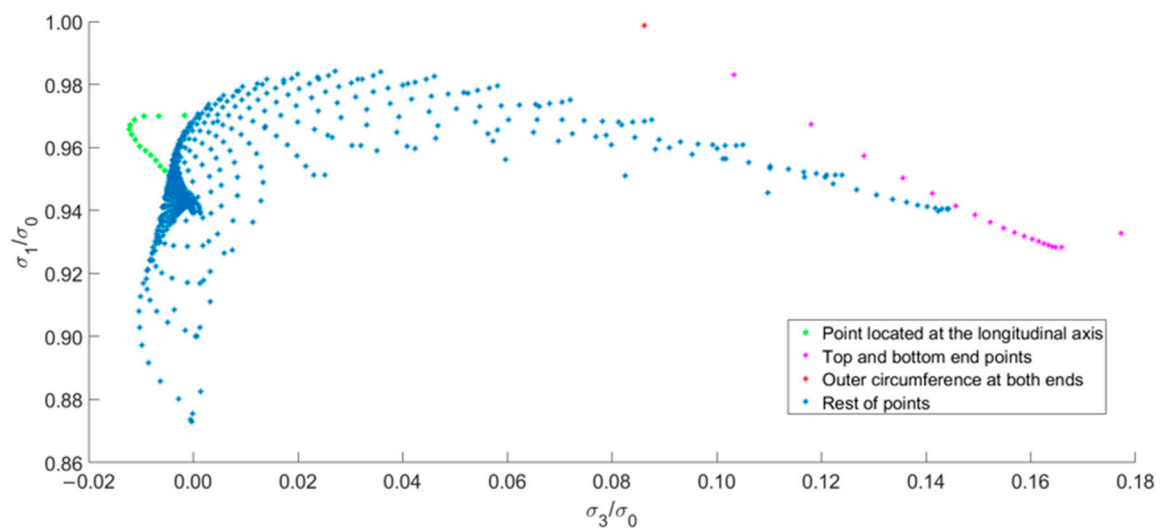


Figure 5. Sets of points of special interest for the case of stiffer platens ($E_p/E_s = 3$).

In the case of the $E_p/E_s = 1$ stiffness ratio, and based on the results shown in Figures 3 and 4, there is no special interest on treating any point or set of points separately, as they are all packed together within a narrow area that, for technical purposes, can be considered as a unique stress state. Therefore, no further considerations were made on pure tensile or compressive points for that case.

The predominance of points located in the tensile area of the $\sigma_1 - \sigma_3$ chart is obtained for the case of softer platens ($E_p/E_s = 0.05$); however, no points of pure tensile stress ($\sigma_3 < 0$ and $\sigma_1 = 0$) are located inside the specimen (Figure 6). Nevertheless, Figure 6 shows a point with an extremely elevated σ_3 tensile value (indicated in green in Figure 6). This is located in the centre of the top and bottom of the specimen's ends, whereas red and blue areas are found in their exterior circumference. Note that these sets of points are the main candidates to initiate failure, as they are closer to the possible tensile failure envelope. Finally, the sets of points highlighted in purple in Figure 6 are those that are also shown in Figure 4 along the vertical axis and depicted with blue dots.

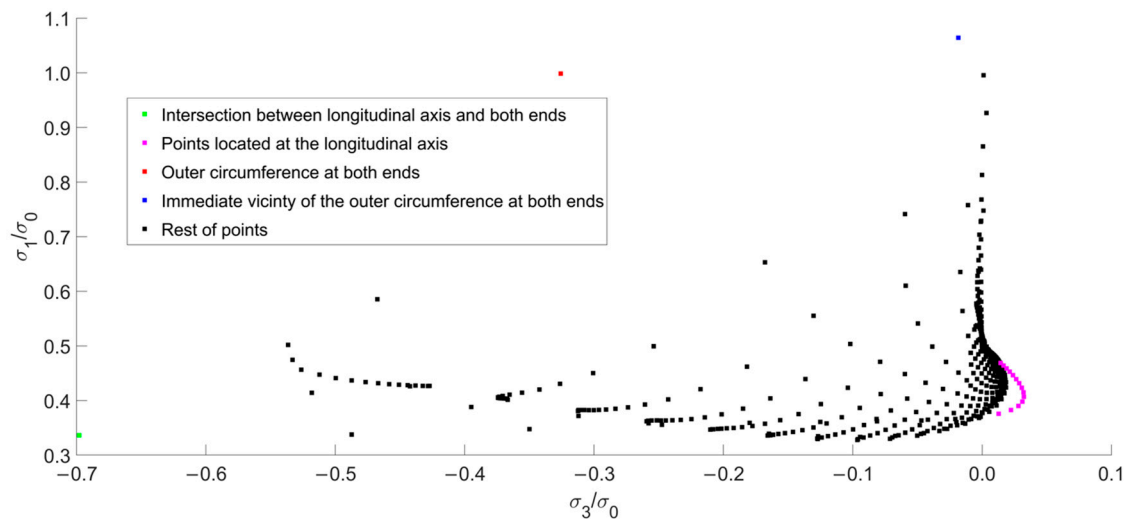


Figure 6. Sets of points of special interest for the case of softer ($E_p/E_s = 0.05$) platens.

3.3. Maximum Shearing Depending on the Material of the Platen

A comprehensive analysis was performed on points of maximum shear stress depending on the platen stiffness. Firstly, it is pertinent to note that no graphical representation of softer platens is depicted in this subsection. This omission is justified by the findings exposed in Section 3.1, wherein it was established that the induced stress field inside the specimen can be considered as a homogeneous compression in which the σ_3 values are neglectable when compared to those of σ_1 . Consequently, from the algebraic expression of maximum shear stresses τ_{max} (Equation (3)), it can be stated that τ_{max} remains nearly constant inside the specimen.

$$\tau_{max} = \frac{|\sigma_1 - \sigma_3|}{2} \tag{3}$$

However, this evidence does not apply for stiffer or softer platens. In these cases, maximum shear stresses should significantly vary, especially in the latter, due to the elevated tensile σ_3 values reached. For stiffer platens ($E_p/E_s = 3$), the distribution of τ_{max} within the specimen is not homogeneous, yet no significant variations were registered across the majority of the sample, as the τ_{max} values were over $0.90\tau_{max_{max}}$, where $\tau_{max_{max}}$ is the maximum τ_{max} value (Figure 7a). Only the immediate vicinity of the contact is under this range and, despite the fact that maximum shear stress is located at a distance of approximately 27.8% from the top and bottom ends due to symmetry, the mid-height area can be considered with constant τ_{max} due to a lower σ_3 value compared to those of σ_1 in that portion of the specimen. This last statement is consistent with the results discussed in Section 3.1.

For softer platens ($E_p/E_s = 0.05$), elevated tensile values of σ_3 are induced, leading to a completely different distribution of τ_{max} inside the specimen (Figure 7b). The appearance of a significant tensile stress field located in the vicinity of the contact suggests that maximum τ_{max} values are concentrated in this area. In fact, even if a threshold of $0.50\tau_{max_{max}}$ is considered, only points near both ends are over it (Figure 7b). Consequently, Figure 7b proves the existence of a pronounced τ_{max} gradient near the outer circumference of both ends, which may induce undesired local failures that eventually affect the trustfulness of the obtained test results.

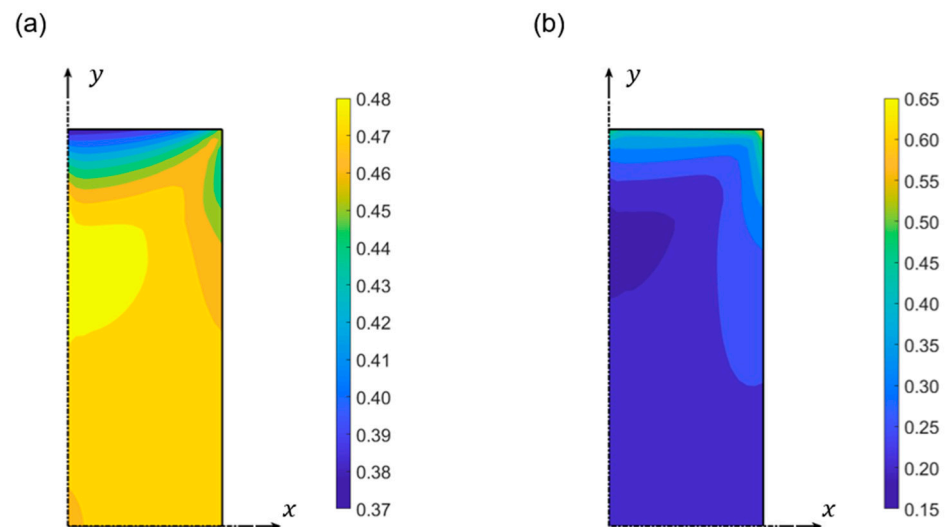


Figure 7. Maximum normalized shear (τ_{max}/σ_0) stress distributions inside the specimen for (a) stiffer ($E_p/E_s = 3$) and (b) softer ($E_p/E_s = 0.05$) platens.

4. Platen Stiffness Influence on Failure Criterion

The UCT is aimed at determining the UCS of a given material. Within this context, it may be argued that only failure criteria on the compressive area of the $\sigma_1 - \sigma_3$ chart would be sufficient to address the failure initiation point in standardized UCT specimens. However, based on the results shown in Section 3, it becomes imperative to consider potential tensile failure in the analysis of the failure initiation point. Thus, even if the aim of this test is to provoke failure of the specimen in a point with coordinates $(\sigma_3, \sigma_1) = (0, UCS)$, meaning that in the ideal scenario no stresses other than compressive stress will be induced, it is essential to verify this scenario for all feasible combinations of relative stiffness. The tensile strength of most brittle materials is not determined by the direct tensile test, but by the Brazilian test. Therefore, the stress state in the failure initiation point is no longer uniaxial; in fact, it is subjected to biaxial stress where $(\sigma_3, \sigma_1) = (-\sigma_{BD}, 3\sigma_{BD})$. It is worth mentioning here that this last statement is widely accepted among the scientific community when failure is initiated at the centre of the specimen, which is only the case for certain contact conditions [12,49]. Furthermore, even in those cases where the failure initiation point is located in the centre of the specimen, deviations from the accepted ratio $\sigma_3/\sigma_1 = -3$ arise as a function of the contact length between the specimen and the jaw during test execution [7].

The failure envelope of each material in the tensile area ($\sigma_3 < 0$) was defined by a linear criterion that connects the points $(\sigma_3, \sigma_1) = (0, UCS)$ and $(\sigma_3, \sigma_1) = (-\sigma_{BD}, 3\sigma_{BD})$ of the material. Consequently, the stress state regarding the Brazilian test is placed in the $\sigma_1 - \sigma_3$ chart, considering that failure is initiated in the centre of the specimen, and that the influence of the contact length is negligible. Hence, the failure envelopes for the compressive and tensile areas are defined by Equation (1)—the Mohr–Coulomb criterion—and Equation (4), respectively.

$$\sigma_1 = \frac{UCS - 3\sigma_{BD}}{\sigma_{BD}}\sigma_3 + \sigma_c \quad (4)$$

To understand how failure is initiated under varied contact conditions, the interactions between the induced stress field and the failure criteria for each case must be carefully analysed. Firstly, interactions between stress states and the failure envelope in the tensile area were addressed (Figure 8). In the case of stiffer platens ($E_p/E_s = 3$), its characteristic tensile bulb suggests that failure is likely reached in the tensile area rather than in the compressive one ($\sigma_1 > 0$). Furthermore, the failure initiation point correlates with significantly high negative σ_3 values located far from the desired vicinity of the σ_1 axis;

this yields results that diverge significantly from the intended uniaxial stress state. For all considered limestone specimens, the failure initiation point is located at the vertical axis and at a distance of approximately 16.7% of the total length of the specimen from both ends, with a ratio $\sigma_3/\sigma_1 = -0.0132$. This result applies independently of the failure criterion used, so even when the Mohr–Coulomb criterion is lengthened from the compressive to the tensile area, the predicted failure initiation remains unchanged and fails due to the existence of a σ_3 stress component that deviates testing results from the originally desired uniaxial stress state.

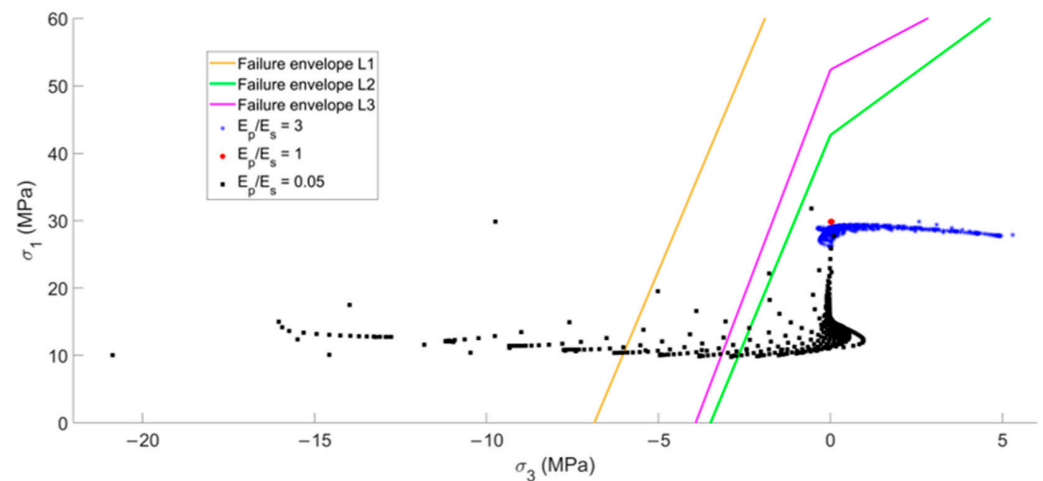


Figure 8. Stress states for (*) steel, aluminium (○) and PMMA (□); and failure envelopes for (orange) L1, (green) L2 and (magenta) L3 materials.

In contrast, the $E_p/E_s = 1$ ratio induced a stress state in the failure initiation point that can be assumed to be uniaxial compression for practical purposes. Additionally, it is located in the compression area, thereby eliminating the influence of tensile stresses on the obtained strength and establishing a stronger relation with the theoretical foundations of the test. Nevertheless, it is worth reiterating that the load ratio highly encourages one to take these results as the real UCS value for any further engineering applications. As the failure is always initiated in the compression area of the $\sigma_1 - \sigma_3$ plot, no tensile failure envelope needs to be considered.

Independently of the failure criterion chosen, all the materials reached failure by the influence of tensile stresses in the case of softer platens ($E_p/E_s = 0.05$). Even if only the Mohr–Coulomb criterion is used for the compressive region, but lengthened to the tensile area, the specimen reaches failure in the tensile area of the $\sigma_1 - \sigma_3$ chart. In that case, the stress ratio at the failure initiation point is $\sigma_3/\sigma_1 = -2.06$, indicating that tensile stress surpasses compressive stress significantly, exceeding reasonable limits to correlate the result with the uniaxial compressive strength of the material. Consequently, it is not recommended to use platens that are significantly less stiff than the tested specimen. It is worth mentioning that softer platens would induce failure in all considered materials, whereas the rest of the platens would not induce failure in any of the specimens.

Figure 9 simultaneously shows the failure envelope for the tensile and compressive areas for all considered rock materials. In addition, it not only includes the stress states previously used in Section 3 and up to this point in Section 4, but also those incremented by a factor of 5, the approximate moment in which failure is reached by compression in the case of softer ($E_p/E_s = 0.05$) platens (Figure 9). Stress fields prove that failure is caused by the existence of a tensile stress component σ_3 in stiffer ($E_p/E_s = 3$) and softer ($E_p/E_s = 0.05$) platens.

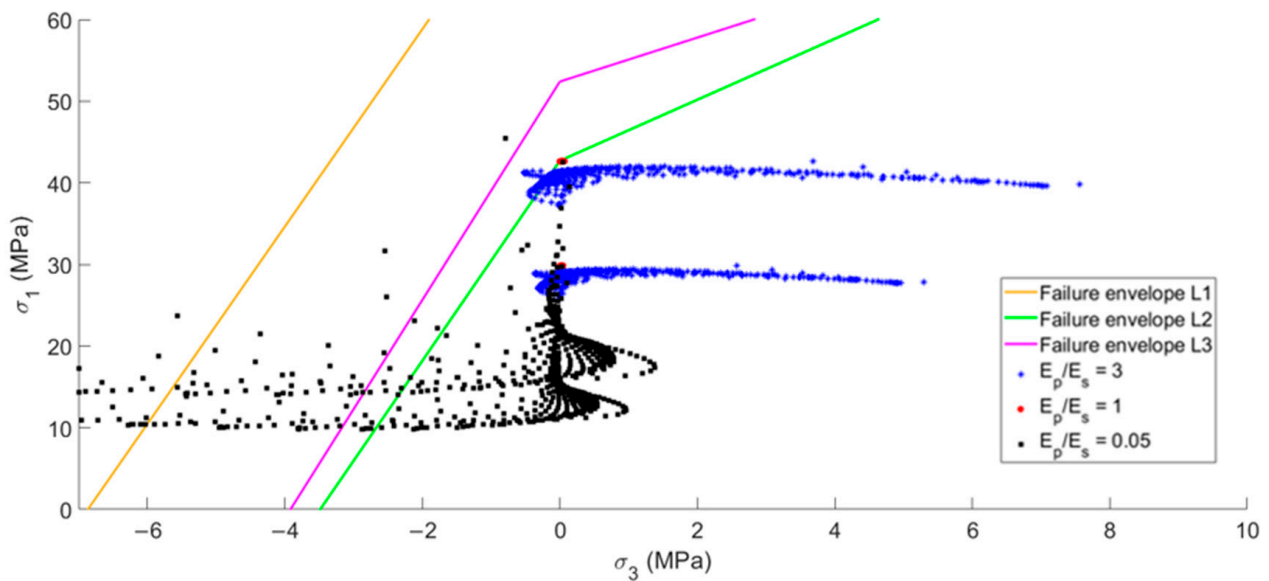


Figure 9. Stress states for (*) stiffer ($E_p/E_s = 3$), (○) equal stiffness ($E_p/E_s = 1$) and (□) softer ($E_p/E_s = 0.05$) platens for two different load levels; and failure envelopes for (orange) L1, (green) L2 and (magenta) L3 limestones.

Correlating previous initiation failure points within the $\sigma_1 - \sigma_3$ chart with their actual coordinates (x, y, z) inside the specimen provides meaningful insights into the predominant failure patterns usually documented as the test output. In the case of stiffer platens ($E_p/E_s = 3$), the generated failure pattern exhibits a characteristic cone shape (Figure 10a). This result applies independently of the failure criterion used (tensile or compressive), so even when the Mohr–Coulomb criterion is lengthened from the compressive to the tensile area, the predicted failure initiation point remains unchanged and fails due to the existence of a σ_3 stress component that deviates testing results from the uniaxial stress state originally desired.

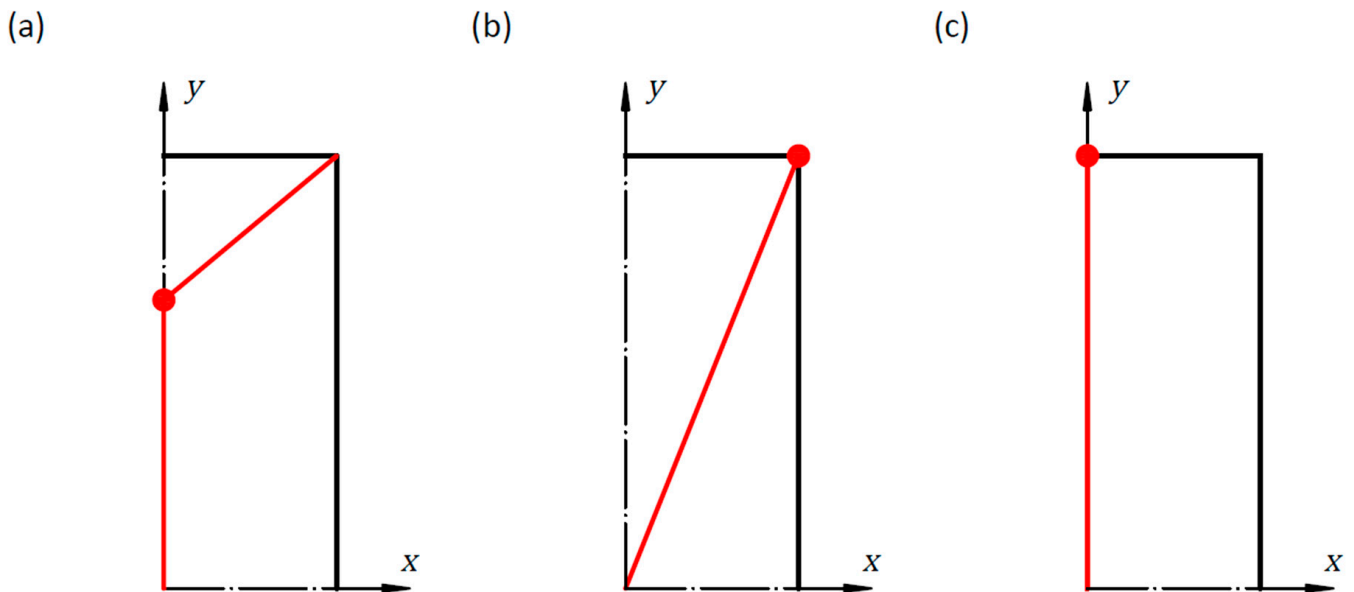


Figure 10. Most common failure initiation points in the cases of (a) stiffer ($E_p/E_s = 3$), (b) equally stiff ($E_p/E_s = 1$) and (c) softer ($E_p/E_s = 0.05$) platens.

Platens with the same stiffness as the tested material ($E_p/E_s = 1$) induced a stress field inside the specimen that initiates failure at the outer circumference of both ends, generating

a failure pattern defined by an oblique plane that connects them (Figure 10b). Therefore, all the similar failure patterns strongly suggest that failure is reached in the compression area and in a uniaxial stress state. This evidence facilitates a preliminary assessment of test validity results without needing any additional tools.

In Figure 10c, the location of the failure initiation point for the case of softer platens ($E_p/E_s = 0.05$) is depicted. This point is situated along the longitudinal axis of the specimen, suggesting a failure plane that contains this axis and splits the specimen into two symmetrical halves. Consequently, the induced stress state highly correlates with the phenomenon of axial splitting during the execution of the test.

The findings presented in this section apply for the materials described in Table 2. Although they cover a wide spectrum of material properties, a straightforward extrapolation of these results to all materials cannot be made, as there is no reason to refuse the possibility of slight differences in the stress field that lead to slightly different failure initiation points in the case of stiffer or softer platens, where points located closer or further to the ends would be acceptable. Nevertheless, it can be ensured that at least three different failure patterns exist, and that they depend on the relative stiffness for specimens with length-to-diameter ratios of 2.5. However, this affirmation can reasonably be extended to those cases where a specimen's slenderness is sufficiently elevated to guarantee an area of a nearly uniform compressive stress field at the mid height of the specimen, while simultaneously being low enough to preclude buckling effects.

Although the preceding results were derived from numerical simulations, experimental evidence of this phenomena can be found in the current literature. Figure 11, extracted from reference [33], shows the standardized UCT performed on cylindrical and prismatic specimens after modifying the contact conditions. In particular, four different cases were addressed. The reference cases in Figure 11 were executed subject to the recommendations set by the standards, whereas glued, grease, Teflon and brush plates were used to vary the boundary conditions at specimen ends, from impeded horizontal displacement to the complete absence of friction between platen and specimen. In both the cylindrical and prismatic geometries, the experimental results are in obvious agreement with the predictions made by the numerical simulations. The reference and glued sheets show a failure pattern defined by the formation of two cones due to the significantly higher stiffness of the platens and the impeded movement sets by glue in the ends of the specimen. After reducing the influence of friction by using grease, the failure pattern obtained experimentally is an oblique plane joining both top and bottom ends, exactly as in the numerical simulations. It is worth noting that the same material and the greased material used in reference [33] was used to reduce the influence of friction and shearing stresses along the boundaries; consequently, both achieved similar results. Eventually, platens with significantly lower stiffnesses led to axial splitting or failure planes parallel to the longitudinal axis of the specimen, as previously predicted by simulations.

It is important to emphasize that different failure patterns are caused even if the specimen's material is considered to be homogeneous and isotropic. Hence, the influence of platen stiffness in more complex real scenarios may be boosted by additional external factors not considered in this analysis, such as high temperature and melting and freezing cycles.



Figure 11. Different failure patterns for (a) cylindrical and (b) prismatic specimens depending on contact conditions. Extracted from [33] and reproduced with permission from Construction and Building Materials, published by Elsevier, 2022.

5. Conclusions

Numerical simulations were performed to determine the influence of platen stiffness on the induced stress field inside specimens subjected to the standardized uniaxial compression test (UCT). Subsequently, the locations of the expected failure initiation points and their dependence on the induced stress field and their related failure patterns were addressed. The results show that when the relative stiffness between the platen (E_p) and the specimen (E_s) is $E_p/E_s = 3$, a cone-shaped failure pattern caused by tensile failure is produced. Additionally, a compression bulb in the vicinity of the contact due to the impeded horizontal movement in the top and bottom ends of the specimen is generated for this stiffness ratio. Conversely, for $E_p/E_s = 0.05$, the induced tensile stresses are concentrated

in a narrow band in the vicinity of the contact, leading to failure initiation points located along the longitudinal axis of the specimen; therefore, a failure pattern characteristic of axial splitting was generated. However, when the platen and specimen stiffnesses are equal ($E_p/E_s = 1$), a uniform and homogeneous stress field is induced inside the specimen, where maximum stresses σ_1 can be considered constant and σ_3 can be neglected for engineering applications. In this latter case, the failure pattern is formed by an oblique plane joining the outer circumference of both ends of the specimen. Therefore, platen material should not be established independently from the tested material. In fact, platen stiffness should be determined considering the material to be characterized, aiming to ensure a stiffness value as close as possible to that of the specimen's. Furthermore, these results allow one to establish the validity of testing results by a simple visual inspection of the generated failure pattern. Finally, those cases where slippery occurred between platen and specimen points along the contact cannot be addressed, considering the findings exposed in this study, as no relative displacement between points was allowed in the numerical model used. Contrary to this, when lubricants are employed to reduce the influence of shearing stresses at the contact, the results may correspond to the case of equal stiffness ($E_p/E_s = 1$), as no horizontal displacement at the specimen ends is constrained; however, further research on the possible deviations from the treated problem must be carried out to ensure definitive conclusions.

Author Contributions: Conceptualization, C.G.-N.; numerical model, M.-I.Á.-F. and R.G.-M.; methodology, R.G.-M.; formal analysis, M.-I.Á.-F. and D.-J.G.-M., writing—original draft preparation, M.-B.P.-G.; data curation, writing—review, editing and visualization, D.-J.G.-M.; supervision, C.G.-N. All authors have read and agreed to the published version of the manuscript.

Funding: This research was funded by the Ministry of Science and Innovation of Spain through Grant MCIU-19-PGC2018-099695-B-100t, and by Grant MCINN-23-PID2022-142015OB-I00 funded by MCIN/AEI/10.13039/501100011033 and by “ERDF A way of making Europe”.

Data Availability Statement: The data presented in this study are available on request from the corresponding author.

Conflicts of Interest: The authors declare no conflicts of interest.

References

- Hondros, G. The Evaluation of Poisson's Ratio and the Modulus of Materials of a Low Tensile Resistance by the Brazilian (Indirect Tensile) Test with Particular Reference to Concrete. *Aust. J. Appl. Sci.* **1959**, *10*, 243–268.
- Hung, K.M.; Ma, C.C. Theoretical Analysis and Digital Photoelastic Measurement of Circular Disks Subjected to Partially Distributed Compressions. *Exp. Mech.* **2003**, *43*, 216–224. [[CrossRef](#)]
- Ma, C.C.; Hung, K.M. Exact Full-Field Analysis of Strain and Displacement for Circular Disks Subjected to Partially Distributed Compressions. *Int. J. Mech. Sci.* **2008**, *50*, 275–292. [[CrossRef](#)]
- Kourkoulis, S.K.; Markides, C.F.; Chatzizergos, P.E. The Standardized Brazilian Disc Test as a Contact Problem. *Int. J. Rock Mech. Min. Sci.* **2013**, *57*, 132–141. [[CrossRef](#)]
- Markides, C.F.; Pazis, D.N.; Kourkoulis, S.K. Influence of Friction on the Stress Field of the Brazilian Tensile Test. *Rock Mech. Rock Eng.* **2011**, *44*, 113–119. [[CrossRef](#)]
- Markides, C.F.; Pazis, D.N.; Kourkoulis, S.K. The Brazilian Disc under Non-Uniform Distribution of Radial Pressure and Friction. *Int. J. Rock Mech. Min. Sci.* **2012**, *50*, 47–55. [[CrossRef](#)]
- Guerrero-Miguel, D.J.; Álvarez-Fernández, M.I.; García-Fernández, C.C.; González-Nicieza, C.; Menéndez-Fernández, C. Analytical and Numerical Stress Field Solutions in the Brazilian Test Subjected to Radial Load Distributions and Their Stress Effects at the Centre of the Disk. *J. Eng. Math.* **2019**, *116*, 29–48. [[CrossRef](#)]
- Carneiro, F.L.L.B. A New Method to Determine the Tensile Strength of Concrete. In Proceedings of the 5th Meeting of the Brazilian Association for Technical Rules, Sao Paulo, Brazil, 16 September 1943; pp. 126–129.
- Fairbairn, E.M.R. A Tribute to Fernando L. L. B. Carneiro (1913–2001) Engineer and Scientist Who Invented the Brazilian Test. *Mater. Struct.* **2002**, *35*, 195–196. [[CrossRef](#)]
- Guerrero-Miguel, D.J.; Alvarez-Fernández, M.I.; Prendes-Gero, M.B.; González-Nicieza, C. Determination of Uniaxial Tensile Strength of Brittle Materials Using Tubular Samples. In Proceedings of the IOP Conference Series: Earth and Environmental Science, Surakarta, Indonesia, 24–25 August 2021; IOP Publishing Ltd.: Bristol, UK, 2021; Volume 833.

11. Markides, C.F.; Kourkoulis, S.K. Towards Alternative Configurations to Determine the Tensile Strength of Brittle Materials. In Proceedings of the 36th Danubia Adria Symposium on Advances in Experimental Mechanics, Plzeň, Czech Republic, 24–27 September 2019; pp. 99–100.
12. Garcia-Fernandez, C.C.; Gonzalez-Nicieza, C.; Alvarez-Fernandez, M.I.; Gutierrez-Moizant, R.A. Analytical and Experimental Study of Failure Onset during a Brazilian Test. *Int. J. Rock Mech. Min. Sci.* **2018**, *103*, 254–265. [[CrossRef](#)]
13. Bahaaddini, M.; Serati, M.; Masoumi, H.; Rahimi, E. Numerical Assessment of Rupture Mechanisms in Brazilian Test of Brittle Materials. *Int. J. Solids Struct.* **2019**, *180–181*, 1–12. [[CrossRef](#)]
14. ASTM D7012-23; Standard Test Method for Compressive Strength and Elastic Moduli of Intact Rock Core Specimens under Varying States of Stress and Temperatures. ASTM International: West Conshohocken, PA, USA, 2023.
15. ASTM D695-15; Standard Test Method for Compressive Properties of Rigid Plastics. ASTM International: West Conshohocken, PA, USA, 2016.
16. ASTM E9-19; Standard Test Methods of Compression Testing of Metallic Materials at Room Temperature. ASTM International: West Conshohocken, PA, USA, 2019.
17. ASTM C39/39M-21; Standard Test Method for Compressive Strength of Cylindrical Concrete Specimens. ASTM International: West Conshohocken, PA, USA, 2021.
18. UNE-EN 12390-3:2020; Ensayos de Hormigón Endurecido. Parte 3: Determinación de La Resistencia a Compresión de Probetas. Spanish Association for Standardization, UNE: Madrid, Spain, 2020.
19. UNE 22950-1:1990; Propiedades Mecánicas de Las Rocas. Ensayos Para La Determinación de La Resistencia. Parte 1: Resistencia a La Compresión Uniaxial. Spanish Association for Standardization, UNE: Madrid, Spain, 1990.
20. Bieniawski, Z.T.; Bernede, M.J. Suggested Methods for Determining the Uniaxial Compressive Strength and Deformability of Rock Materials. *Int. J. Rock Mech. Min. Sci. Geomech. Abstr.* **1979**, *16*, 137–140. [[CrossRef](#)]
21. Broch, E.; Franklin, J.A. The Point-Load Strength Test. *Int. J. Rock Mech. Min. Sci.* **1972**, *9*, 669–697. [[CrossRef](#)]
22. Franklin, J.A. Suggested Method for Determining Point Load Strength. *Int. J. Rock Mech. Min. Sci. Geomech. Abstr.* **1985**, *22*, 51–60. [[CrossRef](#)]
23. Wei, X.X.; Chau, K.T. Analytic Solution for Finite Transversely Isotropic Circular Cylinders under the Axial Point Load Test. *J. Eng. Mech.* **2002**, *128*, 209–219. [[CrossRef](#)]
24. ASTM D5731-16; Standard Test Method for Determination of the Point Load Strength Index of Rock Application to Rock Strength Classifications. ASTM International: West Conshohocken, PA, USA, 2016.
25. Wang, M.; Wan, W. A New Empirical Formula for Evaluating Uniaxial Compressive Strength Using the Schmidt Hammer Test. *Int. J. Rock Mech. Min. Sci.* **2019**, *123*, 104094. [[CrossRef](#)]
26. Moomivand, H. Development of a New Method for Estimating the Indirect Uniaxial Compressive Strength of Rock Using Schmidt Hammer. *Berg Huettenmaenn. Monatsh.* **2011**, *156*, 142–146. [[CrossRef](#)]
27. Filon, L.N.G. On the Elastic Equilibrium of Circular Cylinders under Certain Practical Systems of Load. *Philos. Trans. R. Soc. Lond. Ser. A Contain. Pap. Math. Phys. Character* **1902**, *198*, 147–233. [[CrossRef](#)]
28. Brady, B.T. An Exact Solution to the Radially End-Constrained. *Int. J. Rock Mech. Min. Sci.* **1971**, *8*, 165–178. [[CrossRef](#)]
29. Al-Chalabi, M.; Huang, C.L. Stress Distribution within Circular Cylinders in Compression. *Int. J. Rock Mech. Min. Sci. Geomech. Abstr.* **1974**, *11*, 45–56. [[CrossRef](#)]
30. Jin, C.; Liu, S.; Xu, P.; Guo, C. Scale Effect Stress–Strain Model of Coal Containing Gas. *J. Braz. Soc. Mech. Sci. Eng.* **2019**, *41*, 147. [[CrossRef](#)]
31. Kotsovos, M.D. Effect of Testing Techniques on the Post-Ultimate Behaviour of Concrete in Compression. *Mater. Constr.* **1983**, *16*, 3–12. [[CrossRef](#)]
32. Stredulová, M.; Lisztwan, D.; Eliáš, J. Friction Effects in Uniaxial Compression of Concrete Cylinders. *Procedia Struct. Integr.* **2022**, *42*, 1537–1544. [[CrossRef](#)]
33. Bandeira, M.V.V.; La Torre, K.R.; Kostas, L.E.; Marangon, E.; Riera, J.D. Influence of Contact Friction in Compression Tests of Concrete Samples. *Constr. Build. Mater.* **2022**, *317*, 125811. [[CrossRef](#)]
34. Hudson, J.A.; Brown, E.T.; Farihurst, C. Shape of the Complete Stress-Strain Curve. In Proceedings of the Thirteenth US Symposium on Rock Mechanics, Stability of Rock Slopes, Urbana, IL, USA, 30 August–1 September 1971; ASCE: Reston, VA, USA, 1971; pp. 773–795.
35. Van Mier, J.G.M. *Fracture Process of Concrete*; CRC Press: Boca Raton, FL, USA, 1997.
36. González-Fernández, M.A.; Estévez-Ventosa, X.; Alonso, E.; Alejano, L.R. Analysis of Size Effects on the Hoek-Brown Failure Criterion of Intact Granite Samples. In Proceedings of the IOP Conference Series: Earth and Environmental Science, Turin, Italy, 20–25 September 2021; IOP Publishing Ltd.: Bristol, UK, 2021; Volume 833.
37. Alejano, L.R.; Estévez-Ventosa, X.; González-Fernández, M.A.; Walton, G.; West, I.G.; González-Molano, N.A.; Alvarellos, J. A Method to Correct Indirect Strain Measurements in Laboratory Uniaxial and Triaxial Compressive Strength Tests. *Rock Mech. Rock Eng.* **2021**, *54*, 2643–2670. [[CrossRef](#)]
38. Alejano, L.R.; Arzúa, J.; Estévez-Ventosa, X.; Suikkanen, J. Correcting Indirect Strain Measurements in Laboratory Uniaxial Compressive Testing at Various Scales. *Bull. Eng. Geol. Environ.* **2020**, *79*, 4975–4977. [[CrossRef](#)]
39. Jaeger, J.C.; Cook, N.G.W.; Zimmerman, R.W. *Fundamentals of Rock Mechanics*, 4th ed.; Wiley-Blackwell: Hoboken, NJ, USA, 2007; ISBN 978-0-632-05759-7.

40. De Vallejo, L.I.G.; Ferrer, M.; Ortuño, L.; Oteo, C. *Ingeniería Geológica*; Prentice Hall: Saddle River, NJ, USA, 2002; ISBN 8420531049.
41. Feng, X.T.; Kong, R.; Zhang, X.; Yang, C. Experimental Study of Failure Differences in Hard Rock Under True Triaxial Compression. *Rock Mech. Rock Eng.* **2019**, *52*, 2109–2122. [[CrossRef](#)]
42. Mogi, K. Effect of the Triaxial Stress System on the Failure of Dolomite and Limestone. *Tectonophysics* **1971**, *11*, 111–127. [[CrossRef](#)]
43. Goodman, R.E. *Introduction to Rock Mechanics*, 2nd ed.; John Wiley & Sons Inc.: Hoboken, NJ, USA, 1981; Volume 18, ISBN 0471812005.
44. Nikolić, M.; Roje-Bonacci, T.; Ibrahimbegović, A. Overview of the Numerical Methods for the Modelling of Rock Mechanics. *Teh. Vjesn.* **2016**, *23*, 627–637. [[CrossRef](#)]
45. Perrone, N.; Kao, R. A General Finite Difference Method for Arbitrary Meshes. *Comput. Struct.* **1975**, *5*, 45–58. [[CrossRef](#)]
46. Brighi, B.; Chipot, M.; Gut, E. Finite Differences on Triangular Grids. *Numer. Methods Partial. Differ. Equ.* **1998**, *14*, 567–579. [[CrossRef](#)]
47. Budynas, R.G.; Nisbett, J.K.; Shigley, J.E. *Shigley's Mechanical Engineering Design*; McGraw-Hill: New York, NY, USA, 2011; ISBN 0073529281.
48. Rabat, Á.; Tomás, R.; Cano, M. Assessing Water-Induced Changes in Tensile Behaviour of Porous Limestones by Means of Uniaxial Direct Pull Test and Indirect Methods. *Eng. Geol.* **2023**, *313*, 106962. [[CrossRef](#)]
49. Alvarez-Fernandez, M.I.; Garcia-Fernandez, C.C.; Gonzalez-Nicieza, C.; Guerrero-Miguel, D.J. Effect of the Contact Angle in the Failure Pattern in Slate Under Diametral Compression. *Rock Mech. Rock Eng.* **2020**, *53*, 2123–2139. [[CrossRef](#)]

Disclaimer/Publisher's Note: The statements, opinions and data contained in all publications are solely those of the individual author(s) and contributor(s) and not of MDPI and/or the editor(s). MDPI and/or the editor(s) disclaim responsibility for any injury to people or property resulting from any ideas, methods, instructions or products referred to in the content.